Fast Implicit Solvers using Stabilized Mixed Approximation

Liao, Qifeng and Silvester, David

2011

MIMS EPrint: **2011.36**

Manchester Institute for Mathematical Sciences
School of Mathematics

The University of Manchester

Reports available from: http://eprints.maths.manchester.ac.uk/
And by contacting: The MIMS Secretary
School of Mathematics
The University of Manchester
Manchester, M13 9PL, UK

ISSN 1749-9097

INTERNATIONAL JOURNAL FOR NUMERICAL METHODS IN FLUIDS
Int. J. Numer. Meth. Fluids 0000; **00**:1–26
Published online in Wiley InterScience (www.interscience.wiley.com). DOI: 10.1002/fld

Fast Implicit Solvers using Stabilized Mixed Approximation

Qifeng Liao[1] and David Silvester [1*]

[1] *School of Mathematics, University of Manchester, Manchester, M13 9PL, United Kingdom.*

SUMMARY

This paper concerns a new class of robust and efficient methods for solving the Navier-Stokes equations for unsteady incompressible flow. In previous work (Kay et al. *SIAM J. Sci. Comput.* 2010; 32:111–128) we established the effectiveness of an implicit time integrator using a stabilized trapezoid rule with an explicit Adams–Bashforth method for error control. The role of the stability of the spatial approximation on the overall accuracy of the implicit solution algorithm is the primary focus here. In particular, the relationship between spatial stabilization and temporal solution accuracy is assessed computationally for the case of the lowest order conforming mixed approximation. Copyright © 0000 John Wiley & Sons, Ltd.

Received . . .

KEY WORDS: Stabilized finite element approximation, Navier-Stokes, implicit time stepping.

1. MOTIVATION

Stabilized low-order spatial approximation is a computationally convenient approach when solving incompressible flow problems using finite element discretization methods. Nevertheless, the interplay between spatial stability and temporal solution accuracy seems to be a somewhat delicate issue. Whilst the role of stabilization in steady state flow problems is more-or-less understood, see for example, Roos et al. [1, ch. 4], the theoretical underpinning for spatially stabilized methods is not so well developed when modelling unsteady flow. This is the motivation for this paper.

There is a contentious issue underlying our study: namely, *why bother with stabilized spatial approximation?* Our results will show that this is an open question — there is no guarantee that improved spatial stabilization enhances solution accuracy when solving transient flow problems. The methodology we consider is the lowest order conforming approximation ($\boldsymbol{Q}_1$–$\boldsymbol{P}_0$). Whilst our

*Correspondence to: School of Mathematics, University of Manchester, United Kingdom. E-mail: d.silvester@manchester.ac.uk

focus is on two dimensions (continuous bilinear velocity and discontinuous constant pressure on rectangles), our conclusions remain valid for the three-dimensional analogue (continuous trilinear velocity and discontinuous constant pressure on bricks). Why might the $\boldsymbol{Q}_1$–$\boldsymbol{P}_0$ methodology be of particular interest? We can think of two reasons: first, higher order approximation methods do not provide higher accuracy when the domain has corners, and second, our theoretical results in [2, chapter 4] show the robustness of stabilized $\boldsymbol{Q}_1$–$\boldsymbol{P}_0$ approximation on highly anisotropic meshes in the case of Stokes flow. Such meshes are typically used when resolving shear layers in convection-dominated flows. Standard (inf-sup) stable mixed approximation methods tend to be much less robust if the elements are highly stretched.

2. DISCRETIZATION OF THE NAVIER–STOKES EQUATIONS

Let Ω be a flow domain in $\mathbb{R}^2$ with a polygonal boundary $\partial\Omega$. We want to solve the following initial–boundary value problem: find the fluid velocity $\vec{u}(\vec{x},t)$ and the pressure $p(\vec{x},t)$ satisfying

$$\frac{\partial \vec{u}}{\partial t} - \nu\nabla^2\vec{u} + \vec{u}\cdot\nabla\vec{u} + \nabla p = 0 \quad \text{in} \quad \Omega\times(0,T], \tag{1}$$

$$\nabla\cdot\vec{u} = 0 \quad \text{in} \quad \Omega\times[0,T], \tag{2}$$

$$\vec{u} = \vec{g} \quad \text{on} \quad \partial\Omega_D\times[0,T], \tag{3}$$

$$\frac{\partial \vec{u}}{\partial n} - \vec{n}p = \vec{0} \quad \text{on} \quad \partial\Omega_N\times[0,T], \tag{4}$$

$$\vec{u}(\vec{x},0) = 0 \quad \text{in} \quad \Omega. \tag{5}$$

Our notation is completely standard: $\nu > 0$ is a viscosity parameter (the inverse of the Reynolds number in a dimensionless setting), $T > 0$ is some final time, $\partial\Omega_D$ is the Dirichlet boundary and $\partial\Omega_N$ is the Neumann boundary such that $\partial\Omega = \partial\Omega_D \cup \partial\Omega_N$ and $\partial\Omega_D \cap \partial\Omega_N = \emptyset$. In this paper, both $\partial\Omega_D$ and $\partial\Omega_N$ are assumed to have positive measure.

For any potential numerical scheme solving (1)–(5), there are three important issues: the spatial discretization, the temporal discretization and the linearization of the quadratic term $\vec{u}\cdot\nabla\vec{u}$. The stabilized adaptive TR (Trapezoid Rule) time stepping method introduced by Kay et al. [3] and the linearisation approach of Simo & Armero [4] that is advocated in [3] is adopted here. A feature of this methodology is that it can be used to solve a demanding problem in "black-box" fashion—that is, without tuning parameters, and not knowing the structure (for example, the Strouhal number) of the long-time solution beforehand. Full details are provided below. The spatial discretization strategy is different to that in [3] however—instead of using stable (Taylor-Hood) approximation[†] we use a stabilized mixed approximation method herein.

[†]See [5, ch. 5] for a full discussion of inf-sup stability and a classification of stable and unstable mixed methods.

Prepared using fldauth.cls
DOI: 10.1002/fld

To get to a semidiscrete version of (1)–(5), we must partition the time interval $[0,T]$ into N subintervals $\{[t_n, t_{n+1}]\}_{0\le n\le N-1}$. We let $k_{n+1} := t_{n+1} - t_n$ denote the current time step and let u^n denote $u(\vec{x}, t_n)$. Following [3], at a general TR step our task is to compute a pair of functions $\vec{u}^{\,n+1} \in \boldsymbol{H}^1_E$, $p^{n+1} \in L^2(\Omega)$, that solve the linearized variational problem

$$\begin{aligned} \frac{2}{k_{n+1}}(\vec{u}^{\,n+1}, \vec{v}) + \nu\,(\nabla\vec{u}^{\,n+1}, \nabla\vec{v}) + (\vec{w}^{\,n+1}\cdot\nabla\vec{u}^{\,n+1}, \vec{v}) \;-\; & (p^{n+1}, \nabla\cdot\vec{v}) \\ = \; & (\frac{\partial\vec{u}^{\,n}}{\partial t}, \vec{v}) + \frac{2}{k_{n+1}}(\vec{u}^{\,n}, \vec{v}), \qquad (6) \\ (\nabla\cdot\vec{u}^{\,n+1}, q) \;=\; & 0, \qquad (7) \end{aligned}$$

for all $(\vec{v}, q) \in \boldsymbol{H}^1_{E_0} \times L^2(\Omega)$. Our notation is conventional: the velocity solution and test spaces are given by

$$\boldsymbol{H}^1_E = \left\{ \vec{u} \in H^1(\Omega)^2 \;\middle|\; \vec{u}^{\,n+1} = \vec{g}^{\,n+1} \text{ on } \partial\Omega_D \right\}, \quad \boldsymbol{H}^1_{E_0} = \left\{ \vec{v} \in H^1(\Omega)^2 \;\middle|\; \vec{v} = \vec{0} \text{ on } \partial\Omega_D \right\},$$

and the convection field in (6) is extrapolated from previous velocity estimates via

$$\vec{w}^{\,n+1} = (1 + \frac{k_{n+1}}{k_n})\,\vec{u}^{\,n} - (\frac{k_{n+1}}{k_n})\,\vec{u}^{\,n-1}.$$

Mixed approximation of (6)–(7) is easily achieved, see [5, ch. 5], and is associated with the construction of finite dimensional spaces X^h_0 approximating $\boldsymbol{H}^1_{E_0}$, and M^h approximating $L^2(\Omega)$. Our focus here is on the lowest order rectangular $\boldsymbol{Q}_1$–$\boldsymbol{P}_0$ approximation with the degrees of freedom shown in Fig. 1. We will, however, compare the $\boldsymbol{Q}_1$–$\boldsymbol{P}_0$ results with those obtained using the higher order $\boldsymbol{Q}_2$–$\boldsymbol{P}_1$ approximation shown in Fig. 2. Thus, for a given a spatial subdivision of rectangular elements, the following fully discretized problem must be solved at every time level: find $\vec{d}^{\,n+1}_h \in X^h_E$ and $p^{n+1}_h \in M^h$, where X^h_E is a finite dimensional approximation of the velocity space with boundary data $\frac{\vec{g}^{\,n+1} - \vec{g}^{\,n}}{k_{n+1}}$, solving the *Oseen* problem:

$$\begin{aligned} 2(\vec{d}^{\,n+1}_h, \vec{v}_h) + \nu\,k_{n+1}(\nabla\vec{d}^{\,n+1}_h, \nabla\vec{v}_h) \;+\; & k_{n+1}(\vec{w}^{\,n+1}_h\cdot\nabla\vec{d}^{\,n+1}_h, \vec{v}_h) - (p^{n+1}_h, \nabla\cdot\vec{v}_h) \\ = \; & (\frac{\partial\vec{u}^{\,n}_h}{\partial t}, \vec{v}_h) - \nu\,(\nabla\vec{u}^{\,n}_h, \nabla\vec{v}_h) - (\vec{w}^{\,n+1}_h\cdot\nabla\vec{u}^{\,n}_h, \vec{v}_h), \qquad (8) \\ (\nabla\cdot\vec{d}^{\,n+1}_h, q_h) \;=\; & 0, \qquad (9) \end{aligned}$$

for all $(\vec{v}_h, q_h) \in X^h_0 \times M^h$, where $\vec{w}^{\,n+1}_h = (1 + \frac{k_{n+1}}{k_n})\vec{u}^{\,n}_h - (\frac{k_{n+1}}{k_n})\vec{u}^{\,n-1}_h$. The velocity and acceleration at t_{n+1} can then be updated via

$$\vec{u}^{\,n+1}_h = \vec{u}^{\,n}_h + k_{n+1}\,\vec{d}^{\,n}_h\,, \quad \frac{\partial\vec{u}^{\,n+1}_h}{\partial t} = 2\vec{d}^{\,n}_h - \frac{\partial\vec{u}^{\,n}_h}{\partial t}. \qquad (10)$$

As discussed in [3], in order to start the time integration a potential flow problem is solved to obtain the initial acceleration: we seek $\frac{\partial\vec{u}^{\,0}_h}{\partial t} \in X^h_E$, $p^0_h \in M^h$, solving the *potential flow* problem:

$$\begin{aligned} (\frac{\partial\vec{u}^{\,0}_h}{\partial t}, \vec{v}_h) - (p^0_h, \nabla\cdot\vec{v}_h) \;&=\; -\nu\,(\nabla\vec{u}^{\,0}_h, \nabla\vec{v}_h) - (\vec{u}^{\,0}_h\cdot\nabla\vec{u}^{\,0}_h, \vec{v}_h), \qquad (11) \\ (\nabla\cdot\frac{\partial\vec{u}^{\,0}_h}{\partial t}, q_h) \;&=\; 0, \qquad (12) \end{aligned}$$

Prepared using fldauth.cls
DOI: 10.1002/fld

for all $(\vec{v}_h, q_h) \in X_0^h \times M^h$. We will return to this problem later.

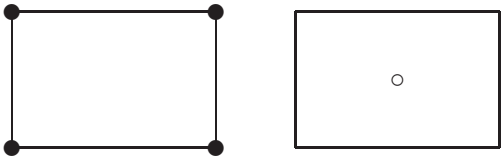

Figure 1. $\boldsymbol{Q}_1$–$\boldsymbol{P}_0$ rectangular element (• velocity node; ∘ pressure).

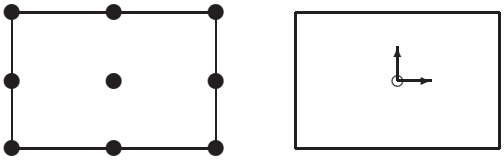

Figure 2. $\boldsymbol{Q}_2$–$\boldsymbol{P}_1$ element (• velocity node; ∘ pressure; $\overset{\uparrow}{\rightarrow}$ pressure derivative).

As is well known, the $\boldsymbol{Q}_1$–$\boldsymbol{P}_0$ approximation is not (inf-sup) stable for arbitrary rectangular grids. For enclosed flow problems (i.e. $\int_{\partial\Omega_N} ds = 0$), the discrete pressure approximation is not even unique up to a constant, due to the so-called checkerboard pressure mode: see [5, pp. 235–238]. For a natural outflow condition with $\int_{\partial\Omega_N} ds > 0$, there is a unique discrete pressure solution, although so-called "pesky pressure modes" see Gresho & Sani [6, pp. 686–691], may still be an issue—especially if ν is large. We will focus on this in Section 3.

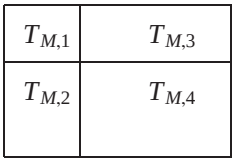

Figure 3. A 2×2 macroelement M.

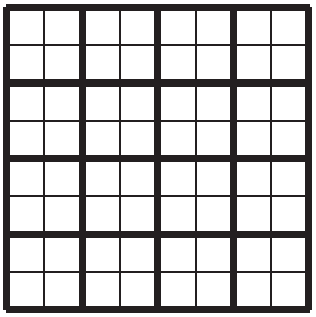

Figure 4. An example of a rectangular partitioning T_h with a macroelement partitioning T_M in bold.

In order to construct a stabilized $\boldsymbol{Q}_1$–$\boldsymbol{P}_0$ approximation, see Kechkar & Silvester [7], the notion of a macroelement needs to be reviewed. A 2×2 macroelement is the union of four neighbouring elements sharing a common vertex. Fig. 3 shows a generic macroelement M which consists

Prepared using fldauth.cls
DOI: 10.1002/fld

of elements $T_{M,i}$, $i = 1:4$ ($\overline{M} = \cup_{i=1:4}\overline{T}_{M,i}$, $M = \overline{M} \setminus \partial\overline{M}$). For a rectangular partitioning T_h, the associated macroelement partitioning is denoted by T_M. An example is shown in Fig. 4. In this paper we assume that any T_h has a unique 2×2 macroelement partitioning T_M associated with it. The framework can easily be extended to more general grids, e.g. by defining a 3×3 or 3×2 macroelement. Thus, a "macroelement" in subsequent sections will always refer to a 2×2 macroelement. Moreover, a (local jump) stabilized $\boldsymbol{Q}_1$–$\boldsymbol{P}_0$ approximation is easily stated. At every TR step we compute $\vec{d}_h^{\,n+1} \in X_E^h$ and $p_h^{n+1} \in M^h$ solving the stabilized Oseen problem:

$$\begin{aligned} 2(\vec{d}_h^{\,n+1}, \vec{v}_h) + \nu\, k_{n+1}(\nabla\vec{d}_h^{\,n+1}, \nabla\vec{v}_h) \;+\; & k_{n+1}(\vec{w}_h^{\,n+1} \cdot \nabla\vec{d}_h^{\,n+1}, \vec{v}_h) - (p_h^{n+1}, \nabla \cdot \vec{v}_h) \\ & = (\frac{\partial \vec{u}_h^{\,n}}{\partial t}, \vec{v}_h) - \nu\,(\nabla\vec{u}_h^{\,n}, \nabla\vec{v}_h) - (\vec{w}_h^{\,n+1} \cdot \nabla\vec{u}_h^{\,n}, \vec{v}_h), \qquad (13) \\ -(\nabla \cdot \vec{d}_h^{\,n+1}, q_h) \;-\; & \beta\,\Upsilon(p_h^{n+1}, q_h) = 0, \qquad (14) \end{aligned}$$

for all $(\vec{v}_h, q_h) \in X_0^h \times M^h$. In (14), β is the stabilization parameter and $\Upsilon(p_h, q_h)$ is given by

$$\begin{aligned} \Upsilon_M(p_h, q_h) \;&:=\; \frac{|M|}{4} \sum_{E \in \Gamma_M} \frac{1}{h_E} \int_E [\![p_h]\!]_E [\![q_h]\!]_E, \qquad (15) \\ \Upsilon(p_h, q_h) \;&:=\; \sum_{M \in T_M} \Upsilon_M(p_h, q_h), \qquad (16) \end{aligned}$$

where Γ_M is the set consisting of the four interior element edges in the macroelement $M \in T_M$, $[\![\cdot]\!]_E$ is the jump across edge E and h_E is the length of E. For further details see [5, p.259]. From Silvester [8], the key idea of the local jump stabilization is to force the pressure approximation to be constant on each macroelement, so that all local checkerboard pressure modes are controlled. The larger the parameter value β is, the closer to a constant on each macroelement the pressure approximation becomes.

For the initial time step, the stabilized method is to find $\frac{\partial \vec{u}_h^{\,0}}{\partial t} \in X_E^h$, $p_h^0 \in M^h$, solving the *stabilized potential flow* problem:

$$\begin{aligned} (\frac{\partial \vec{u}_h^{\,0}}{\partial t}, \vec{v}_h) - (p_h^0, \nabla \cdot \vec{v}_h) \;&=\; -\nu\,(\nabla\vec{u}_h^{\,0}, \nabla\vec{v}_h) - (\vec{u}_h^{\,0} \cdot \nabla\vec{u}_h^{\,0}, \vec{v}_h), \qquad (17) \\ -(\nabla \cdot \frac{\partial \vec{u}_h^{\,0}}{\partial t}, q_h) - \beta\,\Upsilon(p_h^0, q_h) \;&=\; 0, \qquad (18) \end{aligned}$$

for all $(\vec{v}_h, q_h) \in X_0^h \times M^h$.

In our self-adaptive time stepping algorithm, the step sizes $\{k_n\}_{n=1}^N$ are generated using the standard AB2–TR heuristic, see [3]. The other parameters are set as follows:

- initial time step = 10^{-9};
- time stepping tolerance = 10^{-4};
- averaging frequency parameter $n_\star = 10$.

We deliberately take a tiny initial time step. We note that the stabilization in (18) is not absolutely necessary—the system (17)–(18) is solvable with $\beta = 0$. Computational experiments suggest

Prepared using fldauth.cls
DOI: 10.1002/fld

however, that the added stabilization allows the first few time step to increase more quickly—certainly for times shorter than the initial response time referred to in [3]. Our general experience is that the stabilization strategy in (14) does not generate a small time step restriction. This is in contrast to other approaches that have been discussed in the literature, where for transient Stokes problems it is observed that time steps associated with stabilized methods can not be much smaller than the mesh size. For example, Bochev et al. [9] show that, for backward-Euler time stepping, residual based stabilized methods are stable only when $\Delta t > Ch^2$. A detailed study by Burman and Fernández [10] establishes that pressure stabilized methods (including our local jump stabilized method) are unconditionally stable for TR time stepping only if the initial data is regular enough. In the experiments reported here the initial data is zero and regularity of the initial data is assured. The stability of the stabilized Oseen system (13)–(14) for very small time steps in cases when the initial data is rough remains an open question.

The rest of this paper is devoted to numerical results. We will focus on two classical test problems; steady flow over a backward facing step and periodic flow around an obstacle. Both of these problems are hard-wired into our IFISS software toolbox [11], and every experiment reported below can be reproduced by running IFISS with the parameters specified as above.

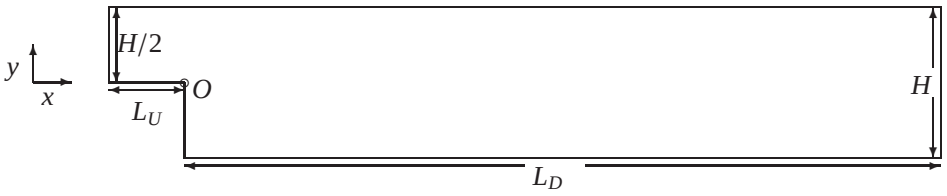

Figure 5. The backward–facing step domain.

3. TEST PROBLEM 1: DESIGN OF THE STABILIZATION PARAMETER

The flow domain for the first test problem is shown in Fig. 5. The corner point O is the origin of the cartesian coordinate system and the dimensions are set so that $H = 2$, $L_U = 1$ and $L_D = 5$. The initial condition (5) implies that the flow is initially at rest. The boundary conditions are set as follows. The Poiseuille velocity profile $\vec{u} = (u, v)$, with

$$u = \left(1 - e^{-10t}\right) 4y(1 - y), \qquad v = 0, \tag{19}$$

is imposed on the inflow boundary (the left boundary), the natural condition (4) is applied on the outflow (the right boundary), and all other boundaries have no-slip and no-penetration so that $\vec{u} = (0, 0)$. The $\boldsymbol{Q}_1$–$\boldsymbol{P}_0$ subdivision is the uniform square mesh with $h = 1/8$, and the $\boldsymbol{Q}_2$–$\boldsymbol{P}_1$ mesh is uniform with $h = 1/4$, so we have the same number of velocity degrees of freedom in both cases.

Prepared using fldauth.cls
DOI: 10.1002/fld

To show the importance of stabilization, pressure solutions at $t = 100$ computed using unstabilized $\boldsymbol{Q}_1$–$\boldsymbol{P}_0$ (i.e. setting $\beta = 0$ in (14)) and with $\boldsymbol{Q}_2$–$\boldsymbol{P}_1$ are shown in Fig. 6 and Fig. 7, respectively. Looking at Fig. 6 we see that when the flow is highly viscous (e.g. $\nu = 1$), the unstabilized $\boldsymbol{Q}_1$–$\boldsymbol{P}_0$ pressure approximation has spurious oscillations in the upstream channel $(-1, 0) \times (0, 1)$ and also in the vicinity of the step corner. In contrast, the $\boldsymbol{Q}_2$–$\boldsymbol{P}_1$ pressure approximation in Fig. 7 is non-oscillatory. Looking more closely at Fig. 6, the spurious pressure oscillations of unstabilized $\boldsymbol{Q}_1$–$\boldsymbol{P}_0$ can be seen to diminish in magnitude as the viscosity parameter is reduced. This suggests that the stabilization parameter should be scaled in proportion to the viscosity in order to avoid over-stabilizing the pressure approximation. From [5, pp. 238–240], we know that the optimal stabilization parameter for stabilized $\boldsymbol{Q}_1$–$\boldsymbol{P}_0$ approximation for the steady-state Stokes problem is $\beta = 1/4$. Thus, we hypothesise that the "best" stabilization parameter in (14) is given by the choice $\beta^\star = \frac{1}{4}\nu$. Note that this design of the stabilization parameter is completely independent of the time step (cf. the residual based stabilization method in [9]). Confirmation of our hypothesis comes from the pressure solutions computed using $\boldsymbol{Q}_1$–$\boldsymbol{P}_0$ with $\beta^\star = \frac{1}{4}\nu$ which are illustrated in Fig. 8. Comparing the reference pressure solutions in Fig. 7 with those shown in Fig. 8 it is difficult to see any difference!

4. TEST PROBLEM 2: STEADY FLOW OVER A STEP FOR REYNOLDS NUMBER 800

4.1. Problem description and logistics

The flow domain for the second test problem is also shown in Fig. 5, but this time we lengthen the outflow so that $H = 2$, $L_U = 1$ and $L_D = 30$. The boundary and initial conditions of test problem 2 are the same as those in test problem 1. If we set the viscosity parameter to the value $\nu = 1/600$ then the flow is expected to remain steady.[‡] There are two pieces of evidence supporting this expectation. First, Gresho et al. [12] performed extensive numerical experiments on a closely related problem which is equivalent to our test problem except that the upstream length L_U is set to zero (or in other words, there is no inlet channel). Their results establish that flow at this Reynolds number ultimately attains a steady-state. Second, the effect of the inlet channel is investigated in detail by Barton [13], where it is shown that for a small viscosity parameter, the inlet channel has only a small influence on the flow field away from the corner. The authors of [13] also point out that for very viscous flow, a long inlet channel could lead to a better agreement between numerical solutions and experimental results. This is the reason we included a non-trivial inlet in our computational model.

Results for two uniform meshes are reported below: one is referred to as the coarse mesh and the other as the fine mesh. For the $\boldsymbol{Q}_2$–$\boldsymbol{P}_1$ approximation, the coarse mesh is uniform with $h = 1/8$

[‡]The parameter value $\nu = 1/600$ corresponds to flow at $Re = 800$ with the standard non-dimensionalisation, see [12].

Prepared using fldauth.cls
DOI: 10.1002/fld

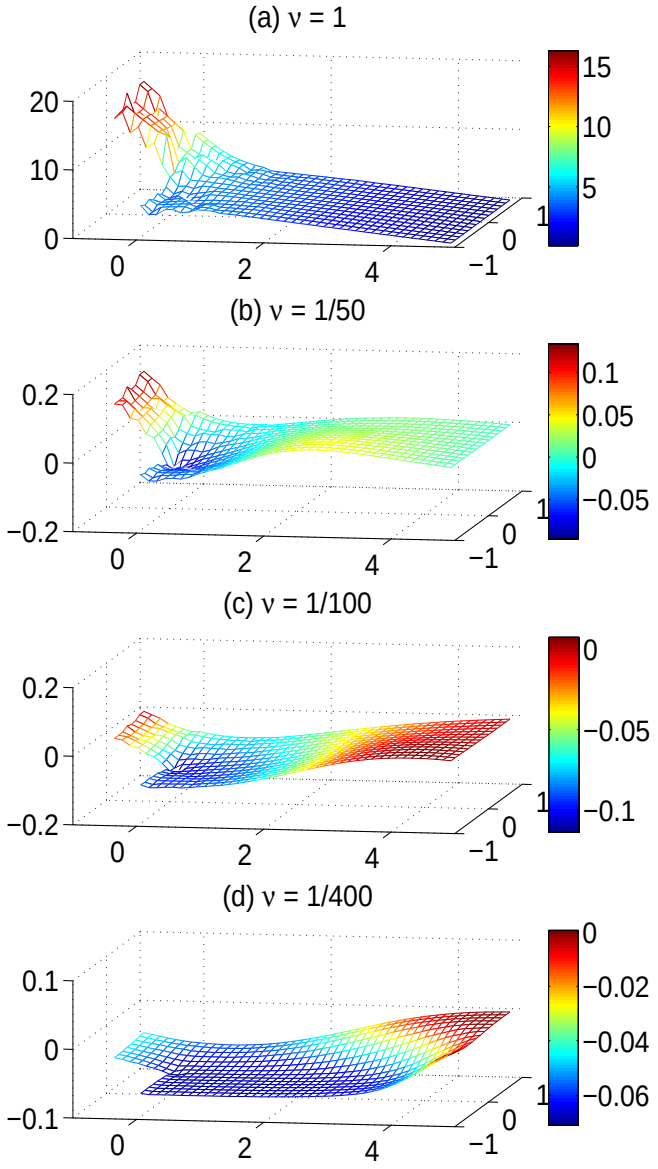

Figure 6. Test Problem 1: Pressure solutions at $t = 100$, computed using $\boldsymbol{Q}_1$–$\boldsymbol{P}_0$ with $\beta = 0$.

(16145 velocity degrees of freedom). The coarse mesh for $\boldsymbol{Q}_1$–$\boldsymbol{P}_0$ approximation, is also uniform with $h = 1/16$. This gives that same velocity degrees of freedom in the two cases. In either case, the fine mesh is obtained by a uniform refinement of the coarse mesh.

The rest of the section is structured as follows: first, visualizations of velocity and pressure fields computed using stabilized $\boldsymbol{Q}_1$–$\boldsymbol{P}_0$ with $\beta = \beta^\star$ will be presented. Subsequently, stabilized and unstabilized results will be compared using the following measures:

- velocity change per time step and the overall kinetic energy;
- time steps generated by our "black-box" time stepping method;

Prepared using fldauth.cls
DOI: 10.1002/fld

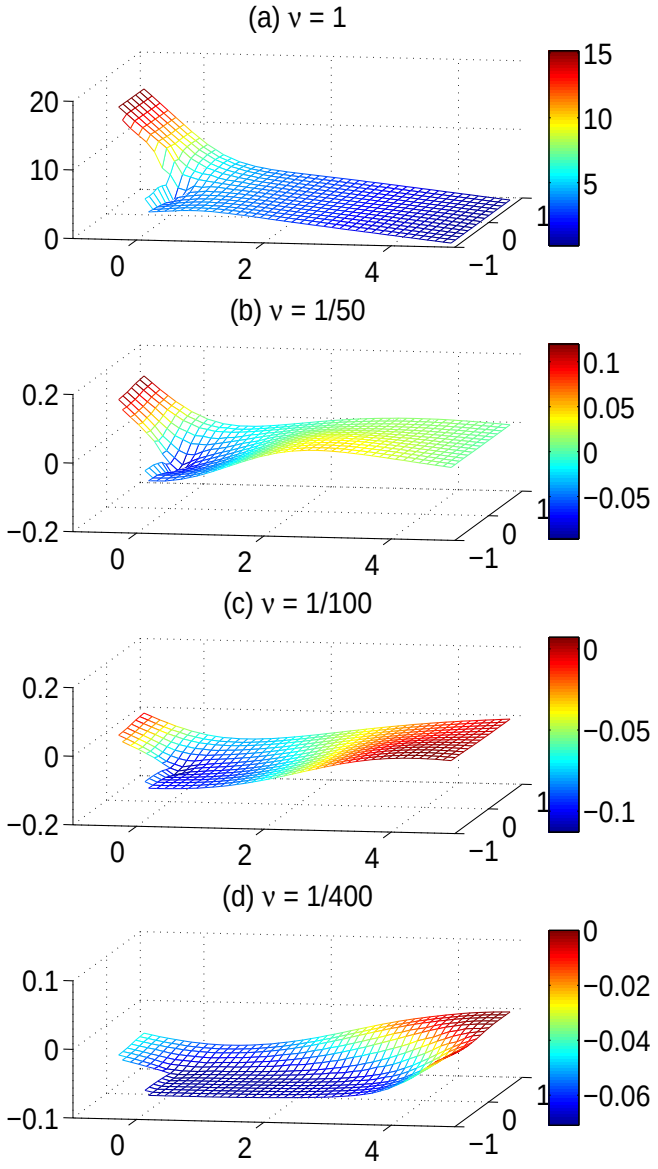

Figure 7. Test Problem 1: Pressure solutions at $t = 100$, computed using Q_2–P_1.

- lengths of the upper and lower eddies;
- velocities and pressures at three history points $\mathbf{P}_1 = (0, 0)$ (the corner), $\mathbf{P}_2 = (10, 0.75)$ (downstream of the step) and $\mathbf{P}_3 = (28, 0)$ (near the outlet) ;
- vorticity and the mean vorticity.

The time interval for computing these quantities is $[0, 450]$. The simulations reported in [12] suggest that this time interval is long enough for the flow to settle down to a steady state.

Prepared using fldauth.cls
DOI: 10.1002/fld

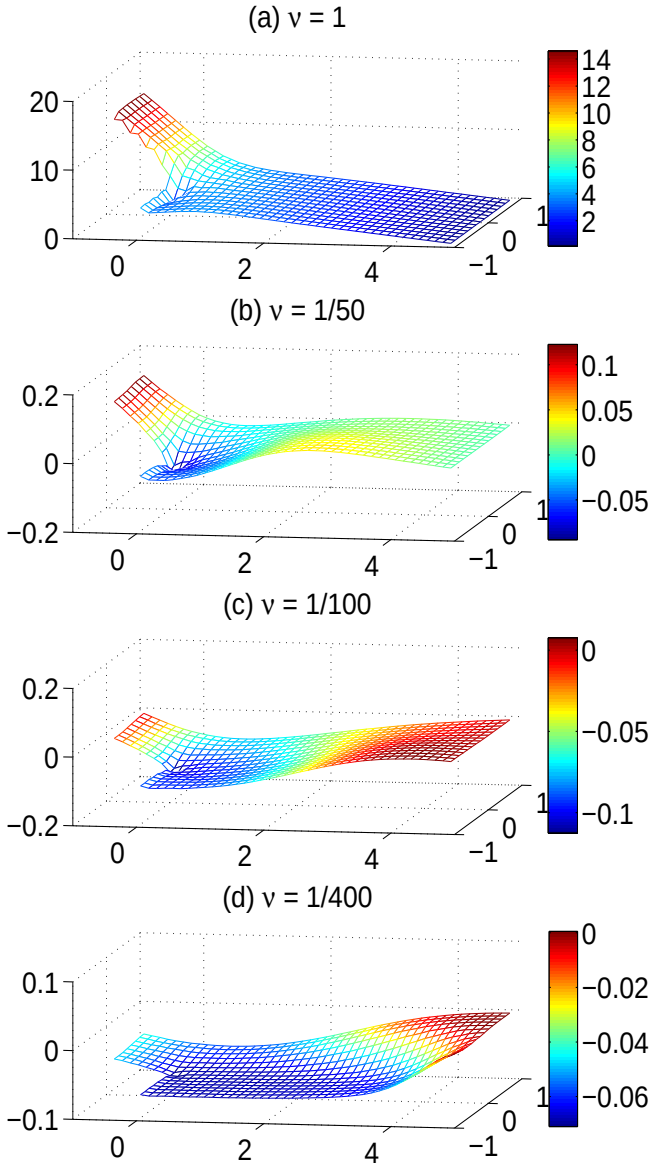

Figure 8. Test Problem 1: Pressure solutions at $t = 100$, computed using $\boldsymbol{Q}_1$–$\boldsymbol{P}_0$ with $\beta = \beta^\star$.

4.2. The flow field at snapshot times

Some reference flow solutions are shown in Fig. 9 to Fig. 12. From Fig. 9(a), at an early time ($t \approx 10$), two separation eddies can be seen clearly—one is the upper eddy and other is the lower eddy. In addition, the upper eddy at this time is quite small and close to the inlet channel. At later times Fig. 9(b) and Fig. 9(c) show that the main upper eddy moves towards the outflow boundary and the lower eddy becomes longer. Also, besides the main eddies, some small eddies appear in these last two pictures. Eventually, in Fig. 10 we see that the main upper and lower eddies become stable features, whereas the other small eddies seem to have dissipated. At time $t \approx 100$, the streamlines

Prepared using fldauth.cls
DOI: 10.1002/fld

close to the outflow boundary are not parallel to the x–axis. The streamlines become closer to parallel at $t \approx 200$, and a "visual" steady-state is reached at $t \approx 450$. The pressure solution evolution is shown in Fig. 11 and Fig. 12. These snapshots show that the pressure changes rapidly at the beginning, but reaches a smooth steady-state profile before the end of the time interval.

4.3. Comparison of stabilized and unstabilized results

In the rest of the section, results will be compared for four alternative approaches:

- A reference $\boldsymbol{Q}_2$–$\boldsymbol{P}_1$ approximation (black);
- Unstabilized $\boldsymbol{Q}_1$–$\boldsymbol{P}_0$ approximation (i.e. $\beta = 0$) (red);
- Optimally stabilized $\boldsymbol{Q}_1$–$\boldsymbol{P}_0$ approximation with $\beta^\star = \frac{1}{4}\nu$ (blue);
- Over-stabilized $\boldsymbol{Q}_1$–$\boldsymbol{P}_0$ approximation with $\beta = \frac{1}{4}$ (green).

The colors will be used to identify the different solutions in the associated figures.

First, Fig. 13 shows the time steps that are generated in the course of the time integration. It can be seen that, independent of the mesh, the time step behaviour for all four approaches are broadly similar. The unstabilized $\boldsymbol{Q}_1$–$\boldsymbol{P}_0$ results (in red) and the optimally stabilized $\boldsymbol{Q}_1$–$\boldsymbol{P}_0$ results (in blue) cannot be distinguished from each other.

A commonly used criterion for assessing when a time dependent flow solution becomes steady is the relative velocity change between successive time steps (see e.g. Barrenechea & Blasco [14]). Typically, the flow is deemed to be steady when the relative change in the velocity is sufficiently small. This measure is assessed in Fig. 14. Note that all four methods ultimately attain a very small relative velocity change (smaller than 10^{-3}). The kinetic energy evolution is shown in Fig. 15. The results computed by all four discretization methods are very close to each other. This suggests that the kinetic energy is a relatively insensitive measure of the spatial accuracy.

We now consider the recirculating eddy structure of the steady flow. There are two separation bubbles in the steady-state flow field (the lower eddy and the upper eddy). To identify their structure some notation is needed. For each x grid value x_k (also, y_k denotes a y grid value), we set

$$u^{up}_{min,x_k} = \min_{y_k}\{u(x,y_k)|\ x = x_k, 0 < y_k < 1\}, \qquad u^{low}_{min,x_k} = \min_{y_k}\{u(x,y_k)|\ x = x_k, -1 < y_k < 0\}.$$

This leads to the simple characterization

$$x^{up}_{in} = \{x_k|\ u^{up}_{min,x_k} < 0\}, \qquad x^{low}_{in} = \{x_k|\ u^{low}_{min,x_k} < 0\}.$$

Thus, for the upper eddy, the starting point is defined by the x grid value which is just smaller than $\min\{x^{up}_{in}\}$ and the reattachment point is $\max\{x^{up}_{in}\}$. The distance between these two points is referred to as the length of the upper eddy. The lower eddy is assumed to start at $x = 0$ and its length is given by $\max\{x^{low}_{in}\}$. The above characterization only makes sense if there is no other eddy except

Prepared using fldauth.cls
DOI: 10.1002/fld

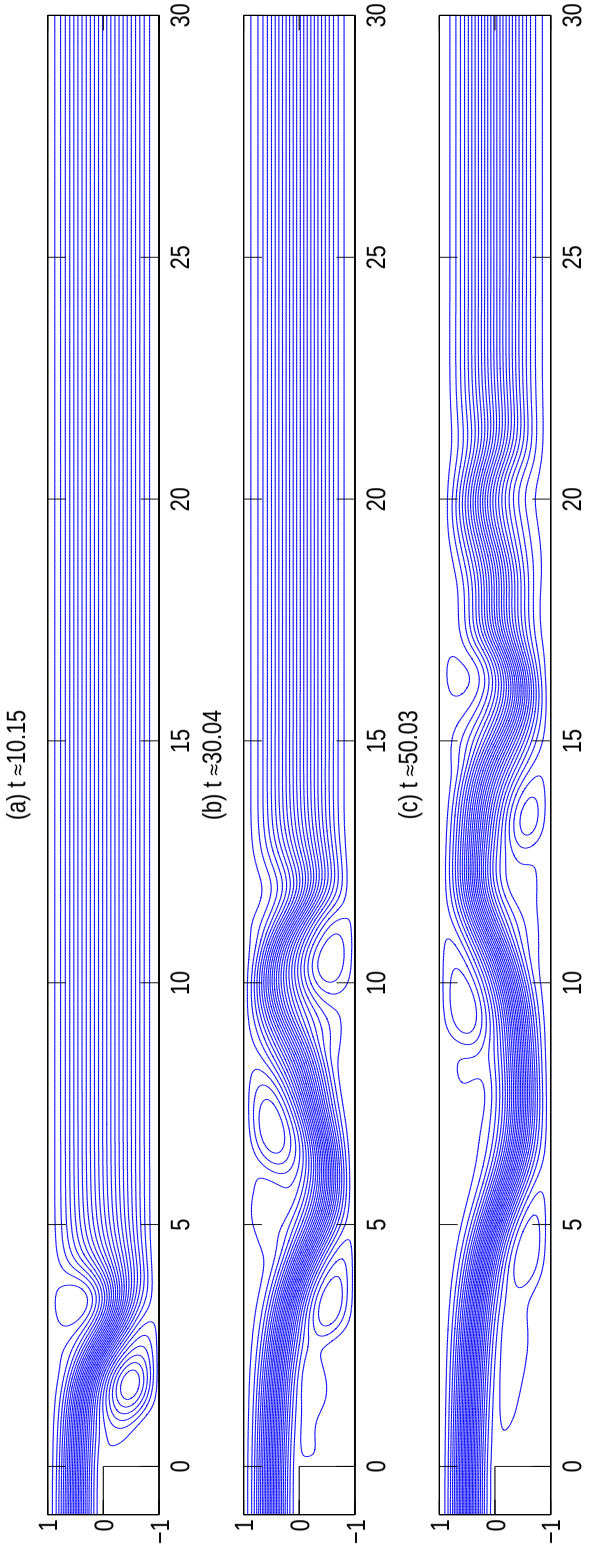

Figure 9. Velocity streamlines generalized by stabilized Q_1–P_0 with $\beta = \beta^\star$ (early time).

DOI: 10.1002/fld

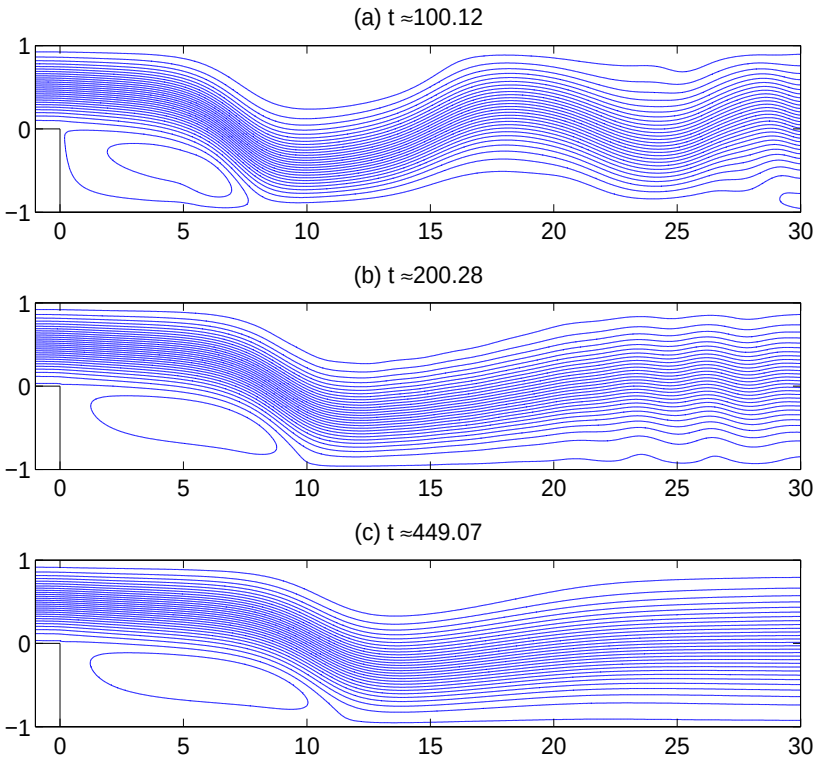

Figure 10. Velocity streamlines generalized by stabilized $\boldsymbol{Q}_1$–$\boldsymbol{P}_0$ with $\beta = \beta^\star$ (long time).

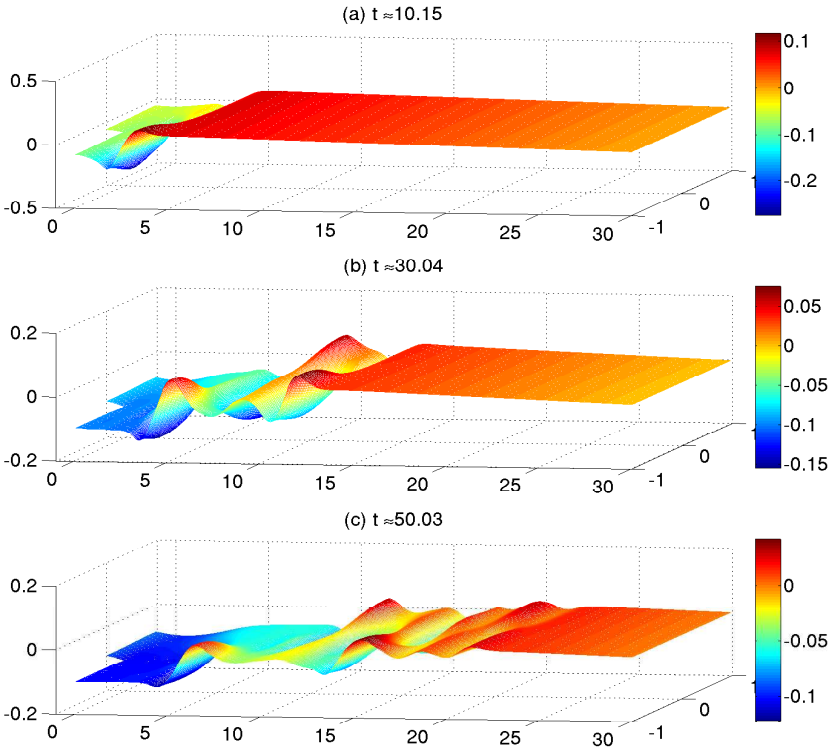

Figure 11. Pressure generalized by stabilized $\boldsymbol{Q}_1$–$\boldsymbol{P}_0$ with $\beta = \beta^\star$ (early time).

Prepared using fldauth.cls
DOI: 10.1002/fld

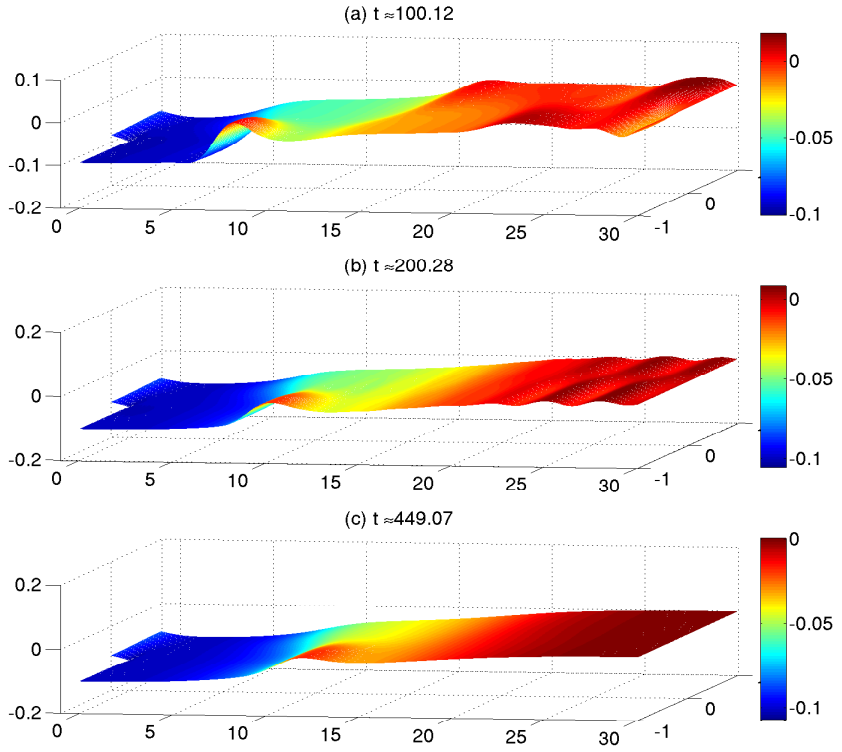

Figure 12. Pressure generalized by stabilized $\boldsymbol{Q}_1$–$\boldsymbol{P}_0$ with $\beta = \beta^\star$ (long time).

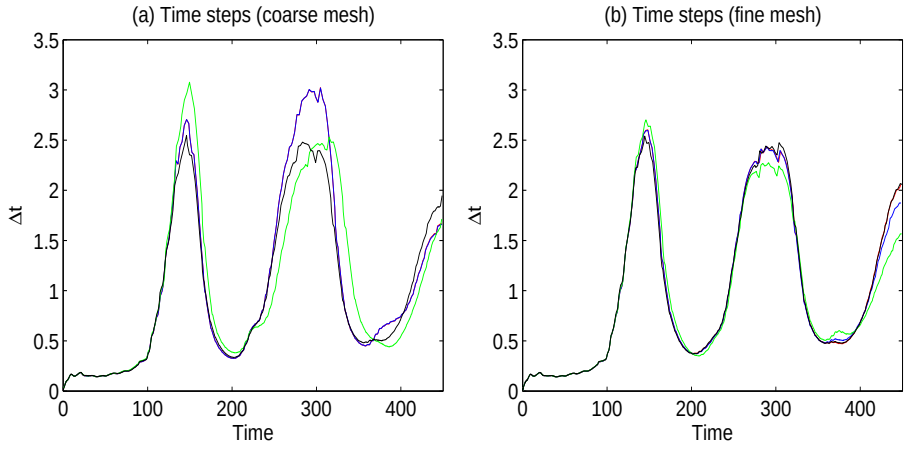

Figure 13. Time step evolution: black is $\boldsymbol{Q}_2$–$\boldsymbol{P}_1$; red is unstabilized $\boldsymbol{Q}_1$–$\boldsymbol{P}_0$; blue is $\boldsymbol{Q}_1$–$\boldsymbol{P}_0$ with $\beta = \beta^\star$; green is $\boldsymbol{Q}_1$–$\boldsymbol{P}_0$ with $\beta = 1/4$.

the main upper and lower eddies, and so is not appropriate when the flow not close to being steady. For this reason, the length of the eddies are only computed for $t > 210$. The time-evolution of the eddies (computed using simple approach above) is shown in Fig. 16. The results with $\beta = 0$ and $\beta = \beta^\star$ are indistinguishable. Two other observations are appropriate. First, on the coarse mesh, the $\boldsymbol{Q}_1$–$\boldsymbol{P}_0$ approximations with $\beta = 0$ or $\beta = \beta^\star$ are much closer to the reference $\boldsymbol{Q}_2$–$\boldsymbol{P}_1$ results than

Prepared using fldauth.cls
DOI: 10.1002/fld

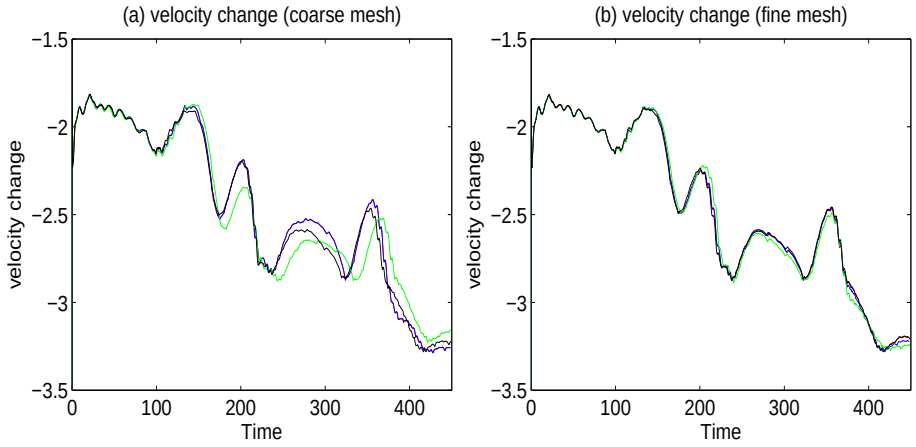

Figure 14. Semi-log plot of $\dfrac{\left\|\vec{u}_h^{n+1}-\vec{u}_h^{n}\right\|_0}{\left\|\vec{u}_h^{n+1}\right\|_0}$.

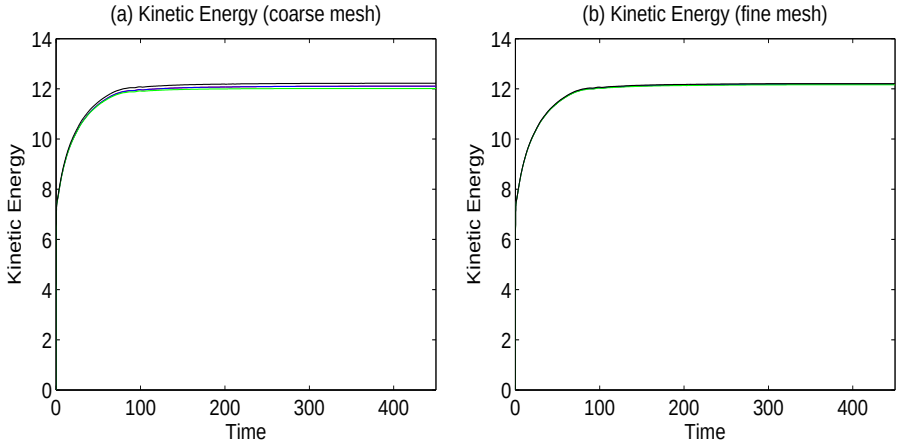

Figure 15. Kinetic energy evolution.

the results with $\beta = 1/4$. Second, all four results are in close agreement when computed using the finer mesh. To give some quantitative information, the reference values provided by Gartling [15] are presented in Table I. These were obtained by directly solving the steady-state problem for the domain with $L_U = 0$. It can be seen that our fine mesh results (at the final time) are slightly smaller than the reference values. This is not so surprising, since as discussed in [13], the blunt inlet channel in [15] is known to give longer separation eddy lengths when the viscosity is small.

Next, the evolution of the horizontal velocity and the vertical velocity at the history points $\mathbf{P}_2$ and $\mathbf{P}_3$ are shown in Fig. 17 and Fig. 18. (The velocity at history point $\mathbf{P}_1$ is simply zero). The pressure evolution at the three history points is shown in Fig. 19. All this point data is in close agreement, except for Fig. 17(c), Fig. 19(a) and Fig. 19(c) where the results with $\boldsymbol{Q}_1$–$\boldsymbol{P}_0$ with $\beta = \frac{1}{4}$ are visually different.

Prepared using fldauth.cls
DOI: 10.1002/fld

Table I. Comparison of fine mesh eddy structure (t=450).

Method	Lower length	Upper start	Upper end	Upper length
Gartling [15]	12.20	9.70	20.96	11.26
$\boldsymbol{Q}_2$–$\boldsymbol{P}_1$	11.4375	9.2812	20.4375	11.1562
$\boldsymbol{Q}_1$–$\boldsymbol{P}_0$ with $\beta = 0$	11.4062	9.2500	20.4375	11.1875
$\boldsymbol{Q}_1$–$\boldsymbol{P}_0$ with $\beta = \beta^\star$	11.4062	9.2500	20.4375	11.1875
$\boldsymbol{Q}_1$–$\boldsymbol{P}_0$ with $\beta = \frac{1}{4}$	11.4062	9.1562	20.3125	11.1562

The final quantity that is compared is the vorticity:

$$\omega = \nabla \times \vec{u} = \frac{\partial v}{\partial x} - \frac{\partial u}{\partial y},$$

with a direction perpendicular to the two dimensional domain. Fig. 20 and Fig. 21 show the contour lines of the vorticity computed using $\boldsymbol{Q}_1$–$\boldsymbol{P}_0$ with $\beta = \beta^\star$. From Fig. 20(a), at $t \approx 10$, the fluid rotation around the step corner is very strong. At $t \approx 30$, it is clear that the vorticity is large in three places: the step corner, the lower eddy reattachment point and the upper eddy reattachment point. When the time becomes very large ($t \approx 450$), the vorticity contour lines seem to reach a steady-state and the main rotation of the flow is at the step corner.

In addition, the mean vorticity ω_Ω which is defined by

$$\omega_\Omega = \int_\Omega \omega,$$

is also computed. Note that, using the Green's theorem,

$$\int_{\partial\Omega} \vec{u} \cdot \vec{t} = \int_\Omega \omega,$$

where $\vec{t}$ is the unit tangential direction on the boundary. Given the imposed flow boundary condition on $\partial\Omega_D$, a non-trivial tangential velocity can only appear on the outflow boundary $\partial\Omega_N$. That is, for all $\vec{u} = (u, v)^T \in \boldsymbol{H}^1_E$,

$$\omega_\Omega = \int_{\partial\Omega_N} v. \tag{20}$$

From (20), the mean vorticity can be used to check the effectiveness of the outflow boundary model. Ideally, the mean vorticity should be to close to zero, i.e. the flow field should be essentially parallel to the horizontal axis. In this situation, the natural condition (4) is valid and has the correct physical meaning—zero pressure on the outflow boundary. In order to achieve this computationally, the downstream channel must be long enough for the flow to "settle". As mentioned earlier, the advice in Gresho et al. [12] is that $L_D = 30$ is long enough for this value of the Reynolds number. The mean

Prepared using fldauth.cls
DOI: 10.1002/fld

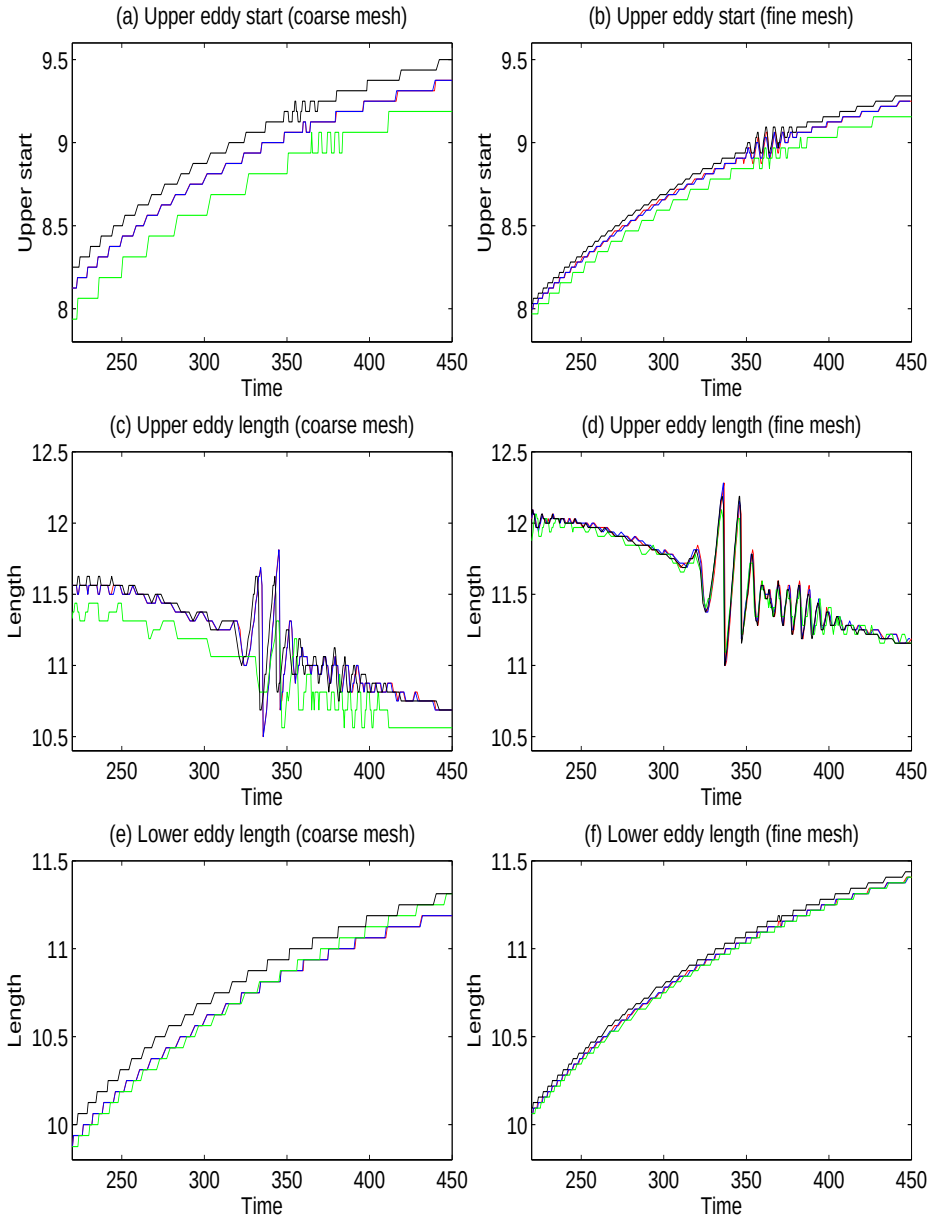

Figure 16. Separation bubbles: black is $\boldsymbol{Q}_2$–$\boldsymbol{P}_1$; red is unstabilized $\boldsymbol{Q}_1$–$\boldsymbol{P}_0$; blue is $\boldsymbol{Q}_1$–$\boldsymbol{P}_0$ with $\beta = \beta^\star$; green is $\boldsymbol{Q}_1$–$\boldsymbol{P}_0$ with $\beta = \frac{1}{4}$.

vorticity evolution is shown in Fig. 22. From this figure, it is clear that the mean vorticity stays close to zero for all time: independent of the approximation methodology. For the fine mesh, the absolute value of the mean vorticity at $t = 450$ lies between 5×10^{-4} and 2×10^{-3} in all cases considered.

DOI: 10.1002/fld

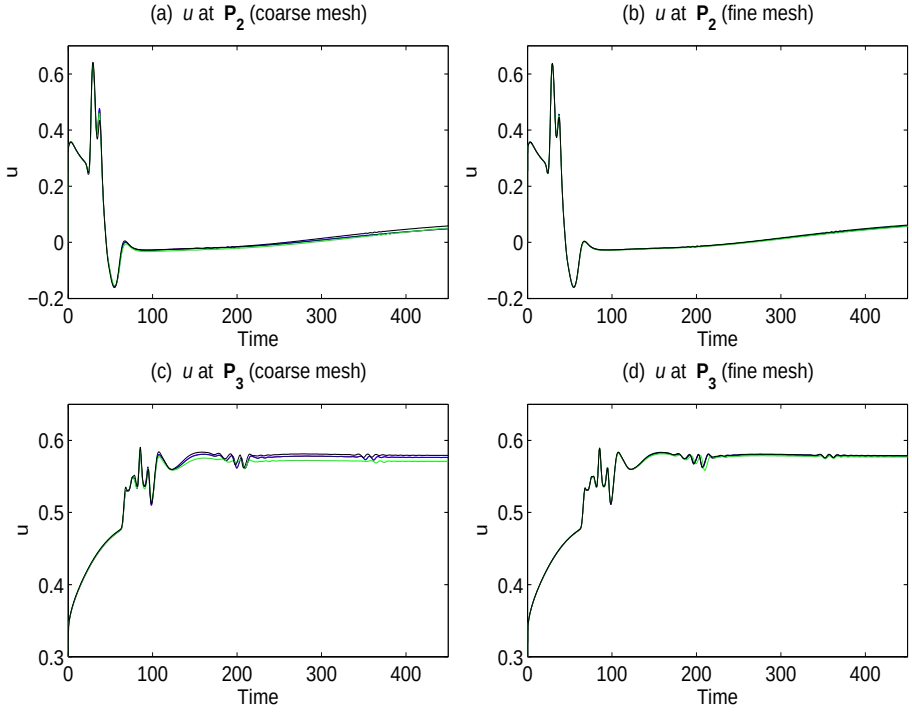

Figure 17. Horizontal velocity at the history points.

4.4. Some linear algebra issues

We conclude this section with a comment about linear algebra aspects. When the adaptive time stepping algorithm was being tested in the IFISS package, two equivalent linear algebra problems representing the system to be solved at every timestep were considered: the standard saddle-point system associated with (6)–(7) or (13)–(14), that is,

$$\begin{bmatrix} F & B^T \\ B & -C \end{bmatrix} \begin{bmatrix} \mathbf{u} \\ \mathbf{p} \end{bmatrix} = \begin{bmatrix} \mathbf{f} \\ \mathbf{g} \end{bmatrix}; \tag{21}$$

or an alternative system that is obtained by rescaling the pressure vector in (21),

$$\begin{bmatrix} F & k_j B^T \\ k_j B & -k_j^2 C \end{bmatrix} \begin{bmatrix} \mathbf{u} \\ \mathbf{q} \end{bmatrix} = \begin{bmatrix} \mathbf{f} \\ k_j \mathbf{g} \end{bmatrix}, \tag{22}$$

where k_j is the time step, and $\mathbf{p} = k_j \mathbf{q}$. Note that although (21) and (22) are mathematically equivalent, solving (22) using the MATLAB sparse "backslash" solver is much faster (often an order of magnitude faster) than solving (21).[§] Thus, the scaled formulation (22) is used for all the numerical experiments in this paper. Using the default "fast solver" in IFISS (preconditioned

[§]The reason for this surprising behaviour is that a different sparse reordering algorithm is applied in the two cases.

Prepared using fldauth.cls
DOI: 10.1002/fld

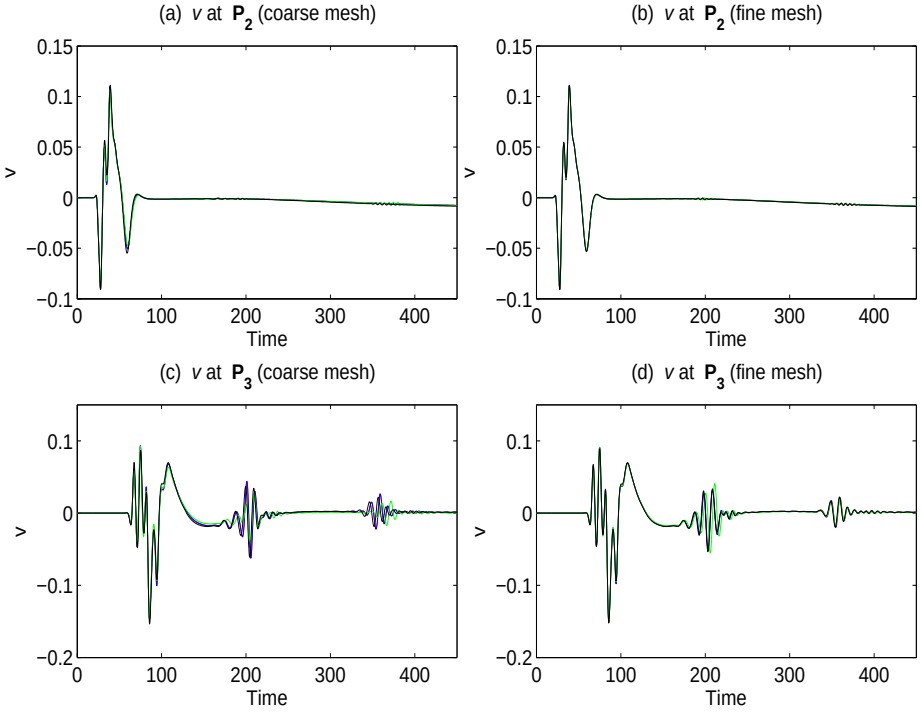

Figure 18. Vertical velocity at the history points.

GMRES with residual reduction of 10^{-5}) in place of "backslash" gives the iteration counts in Table II. It is interesting to note that the standard system is easier to precondition than the rescaled system. Moreover the optimally stabiliized system with $\beta = \beta^\star$ is significantly better conditioned than the (over-stabilized) system with $\beta = 1/4$. Further details of the fast solver technology that is built into IFISS can be found in overview paper by Elman et al. [16].

Table II. Number of preconditioned GMRES iterations at the snapshot time $t = 200$

	Coarse mesh		Fine mesh	
Method	Standard	Rescaled	Standard	Rescaled
Q_2–P_1	15	13	11	10
Q_1–P_0 with $\beta = 0$	5	5	5	5
Q_1–P_0 with $\beta = \beta^\star$	5	10	6	9
Q_1–P_0 with $\beta = \frac{1}{4}$	36	84	33	70

Prepared using fldauth.cls
DOI: 10.1002/fld

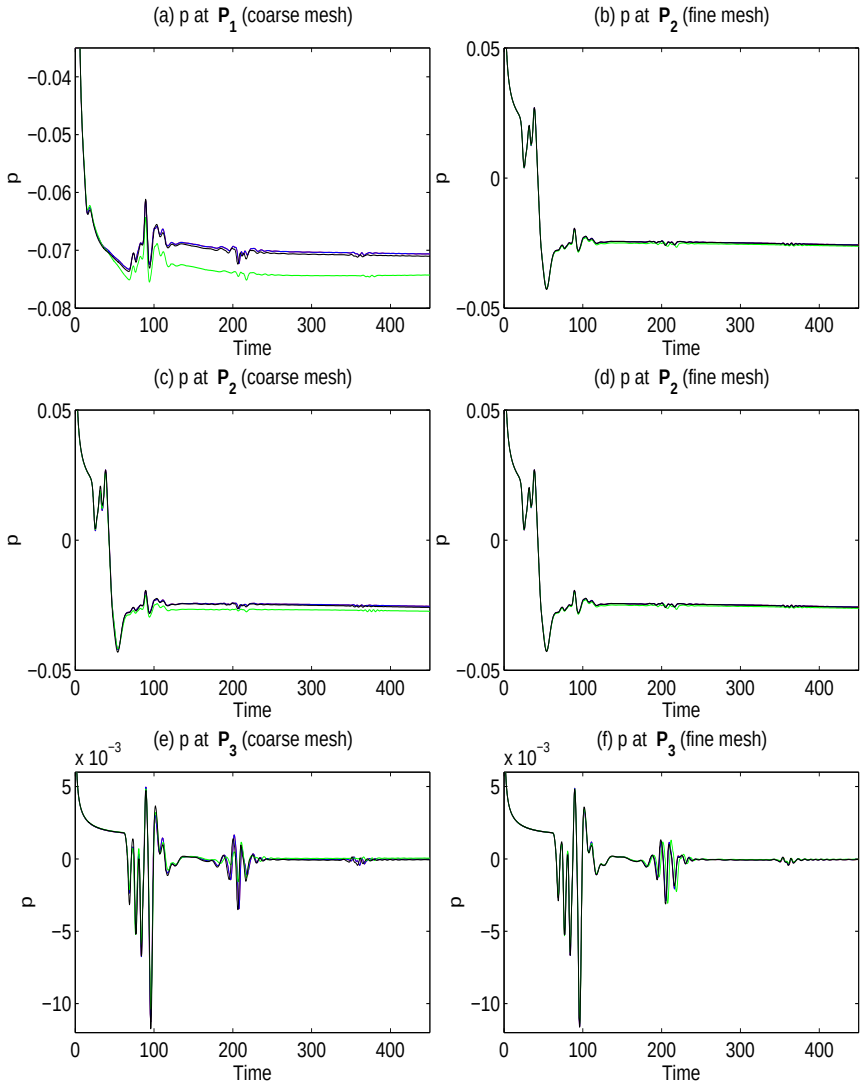

Figure 19. Pressure at history points.

5. TEST PROBLEM 3: PERIODIC FLOW AROUND A SQUARE CYLINDER

Our third test problem is that of flow in a channel around a square cylindrical obstruction. The flow domain is shown in Fig. 23. The cylinder is positioned symmetrically in the center of the channel. The boundary conditions are set as follows. The Poiseuille velocity profile $\vec{u} = (u, v)$, with

$$u = \left(1 - e^{-10t}\right)(1 - y^2), \qquad v = 0, \tag{23}$$

is imposed on the inflow boundary (the left boundary), the natural condition (4) is applied on the outflow (the right boundary), and all other boundaries have no-slip and no-penetration so that $\vec{u} = (0, 0)$. From the work of Sharma & Eswaran [17], the solution of this test problem is known to

Prepared using fldauth.cls
DOI: 10.1002/fld

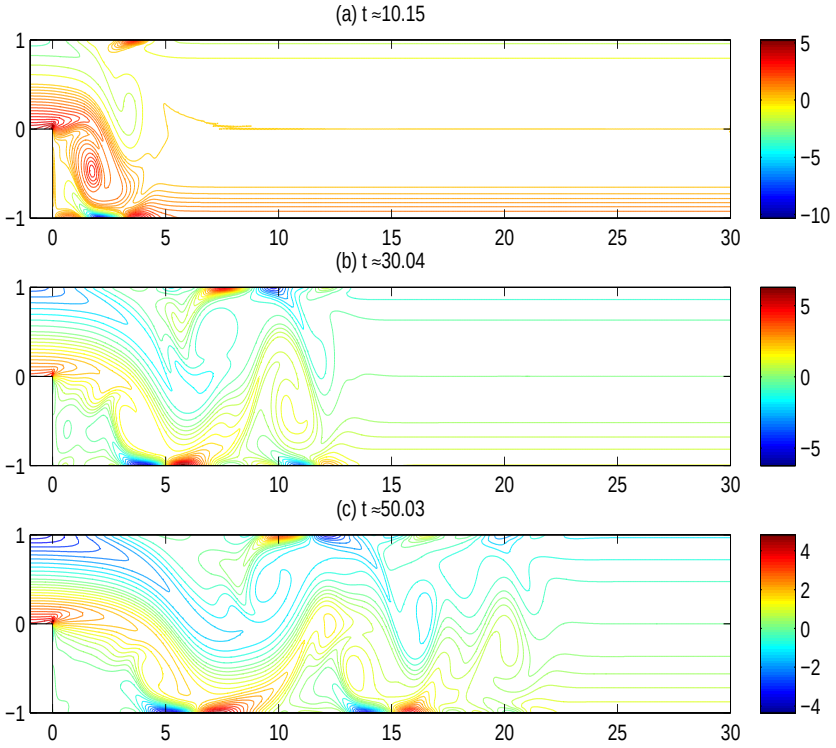

Figure 20. Vorticity computed using Q_1–P_0 with $\beta = \beta^\star$ (early time).

be periodic for $80 < \mathrm{Re} < 320$. Herein, we set the viscosity parameter ν to $1/300$, which led to a periodic solution in every case.

In order to check the performance of the four discretization methods, the drag coefficient C_d and the lift coefficient C_l are computed so that

$$C_d = \int_S (\nu \frac{\partial u_{t_s}}{\partial n} n_y - p n_x), \quad C_l = -\int_S (\nu \frac{\partial u_{t_s}}{\partial n} n_x + p n_y), \tag{24}$$

where S is the surface of the cylinder, $\vec{n} = (n_x, n_y)^T$ is the normal vector on S, $t_s = (n_y, -n_x)^T$ is the tangential vector and u_{t_s} is the tangential velocity. Two kinds of meshes were tested for this flow problem. The first one is a uniform mesh—for Q_2–P_1 it consists of 1008 rectangles, while for Q_1–P_0 it is obtained by unform refinement of the Q_2–P_1 mesh. The second mesh is highly stretched—that used for Q_2–P_1 is shown in Fig. 24. The Q_1–P_0 mesh is again obtained by a single uniform refinement—so the number of velocity degrees of freedom is the same in both cases. The stretched mesh should provide much more accurate drag and lift coefficients than the uniform mesh.

Solving the flow problem using the our time stepping methodology gives the very interesting time step evolution profiles shown in Fig. 25. Note that the time steps vary by four orders of magnitude over the course of the time integration! Although the time steps of our four discretization methods

Prepared using fldauth.cls
DOI: 10.1002/fld

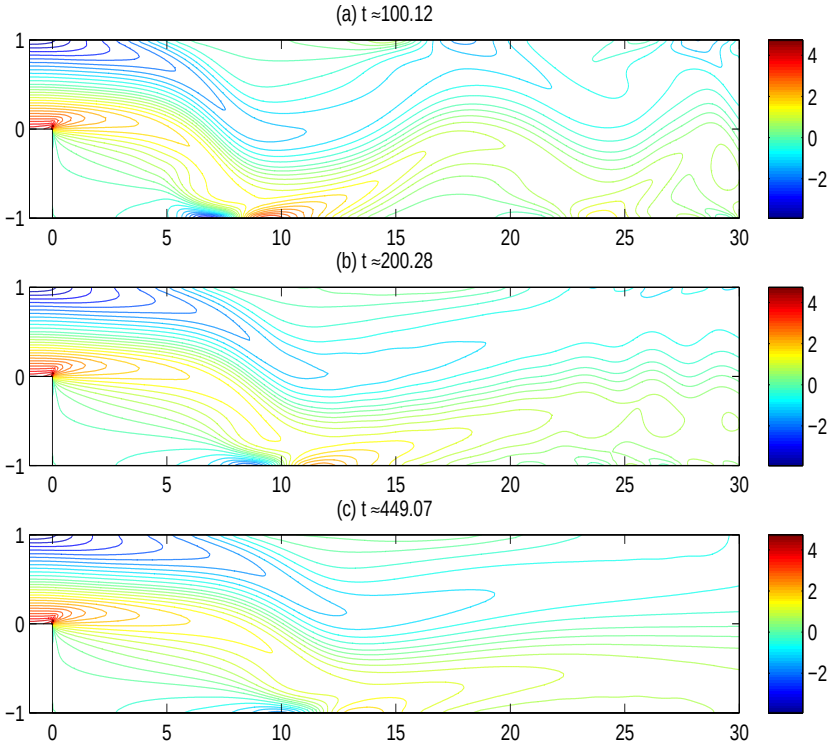

Figure 21. Vorticity computed using $\boldsymbol{Q}_1$–$\boldsymbol{P}_0$ with $\beta = \beta^\star$ (long time).

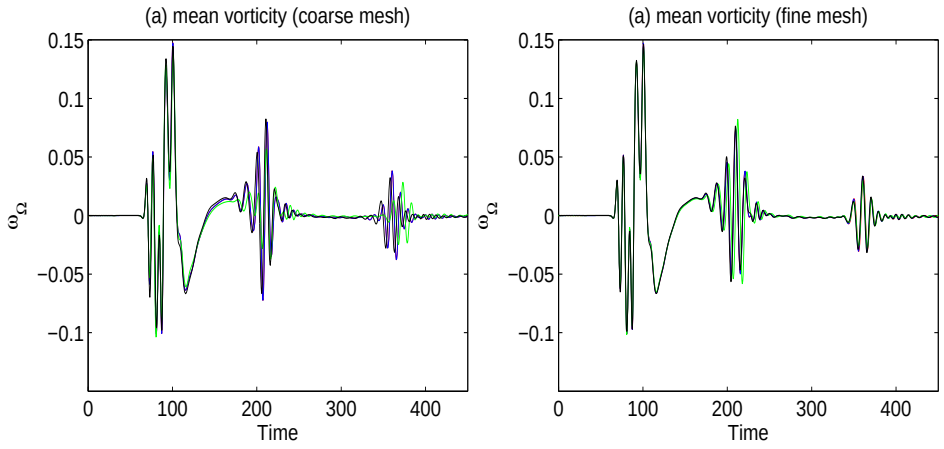

Figure 22. Mean vorticity ω_Ω.

are visually different at early time, they are in perfect agreement when t is large—ultimately the time steps all settle on a value close to 0.03 time units.

Fig. 26 shows the computed drag coefficients. For the stretched mesh, $\boldsymbol{Q}_2$–$\boldsymbol{P}_1$ and $\boldsymbol{Q}_1$–$\boldsymbol{P}_0$ with $\beta = 0$ or $\beta = \beta^\star$ are again in close agreement. Looking at Fig. 26(d) in more detail we find that the $\boldsymbol{Q}_2$–$\boldsymbol{P}_1$ coefficient oscillates between 0.78 and 0.785, whereas the optimally stabilized $\boldsymbol{Q}_1$–$\boldsymbol{P}_0$ coefficient oscillates between 0.795 and 0.80, so the difference is less than 3% of the magnitude. The

Prepared using fldauth.cls
DOI: 10.1002/fld

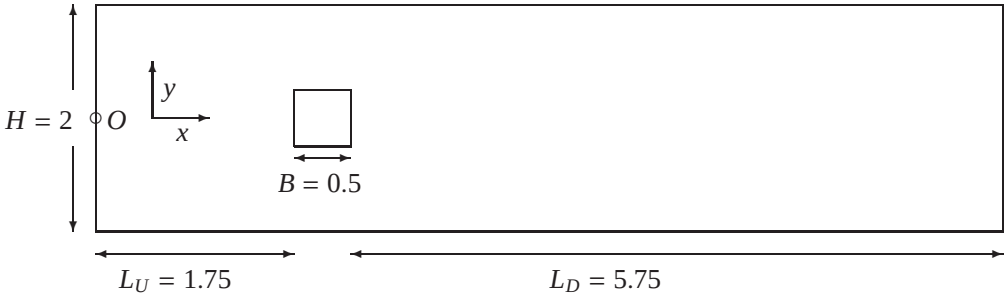

Figure 23. A square cylinder in a channel.

overstabilised Q_1–P_0 results are inaccurate, both qualitatively (especially on the stretched mesh) and quantitatively. Fig. 27 shows the computed lift coefficients. There is good agreement for Q_1–P_0 with $\beta = 0$ or $\beta = \beta^\star$ with the reference Q_2–P_1 values. The results for Q_1–P_0 with $\beta = 1/4$ are qualitatively incorrect. They magnitude of the lift oscillation can be seen to decrease over the time interval rather than remaining constant!

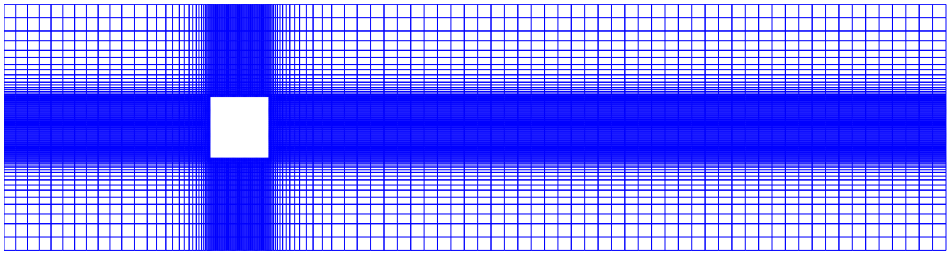

Figure 24. Test problem 3: stretched mesh with 2826 rectangles.

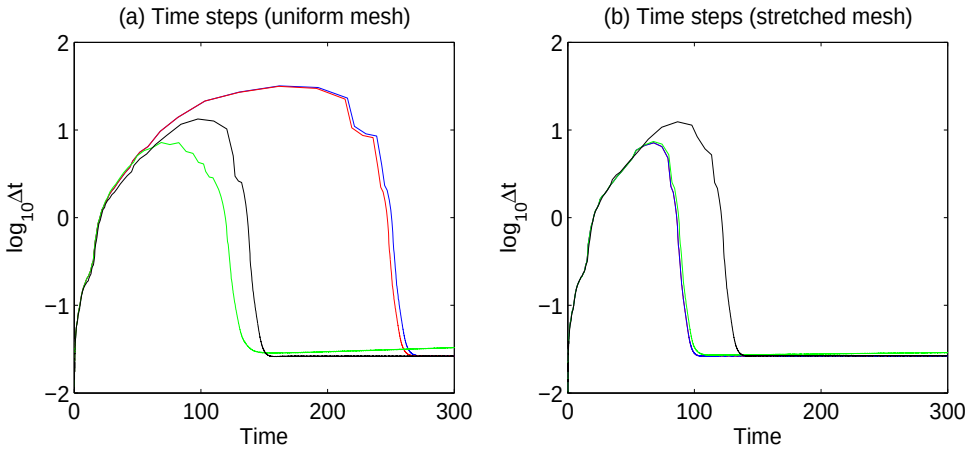

Figure 25. Test problem 3: time step evolution for the four approximation methods.

DOI: 10.1002/fld

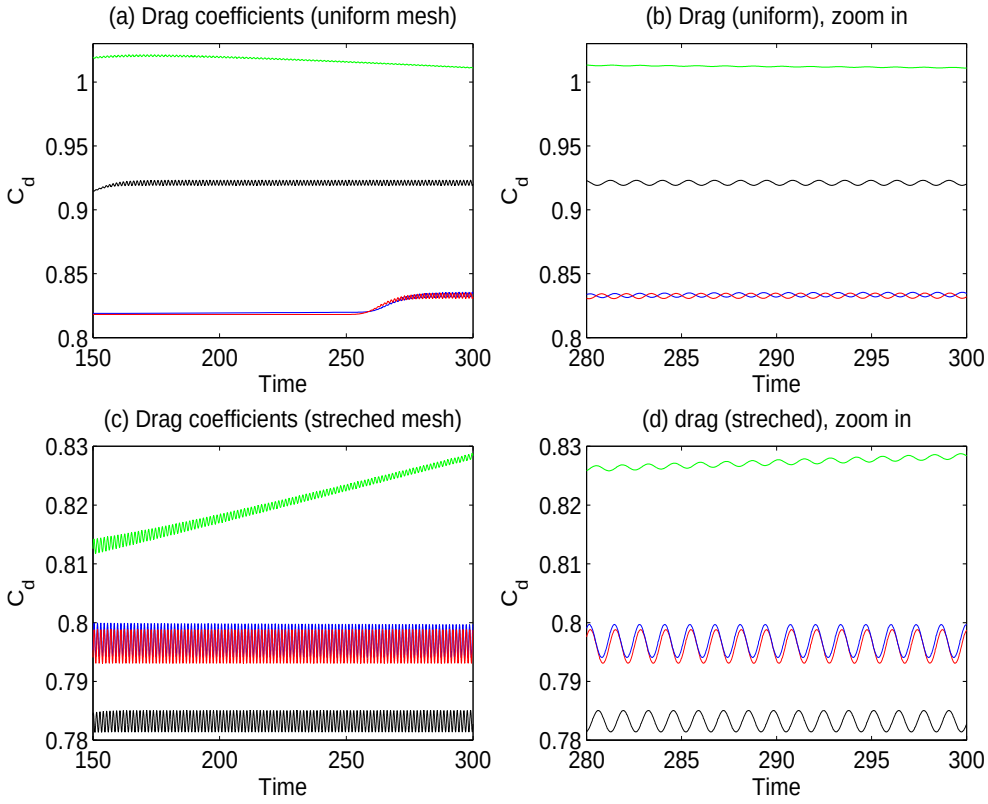

Figure 26. Test problem 3: Drag coefficients.

The periods of the computed lift and drag coefficients (used to define the Strouhal number of the flow) are presented in Table III. Herein, a period is defined by the length of the time interval between two local minima of the oscillation quantities, and is averaged over the final N periods up to the final time. We see that results obtained by averaging over 5 and 10 periods are not significantly different. The optimally stabilized results again show good agreement with the reference results.

Table III. Periods of the drag and lift coefficients on the stretched mesh.

Method	Drag $N = 5$	Drag $N = 10$	Lift $N = 5$	Lift $N = 10$
$\boldsymbol{Q}_2$–$\boldsymbol{P}_1$	1.3203	1.3177	2.6354	2.6354
$\boldsymbol{Q}_1$–$\boldsymbol{P}_0$ with $\beta = 0$	1.3196	1.3236	2.6472	2.6459
$\boldsymbol{Q}_1$–$\boldsymbol{P}_0$ with $\beta = \beta^\star$	1.3226	1.3226	2.6451	2.6464
$\boldsymbol{Q}_1$–$\boldsymbol{P}_0$ with $\beta = \frac{1}{4}$	1.3693	1.3708	2.7421	2.7366

Prepared using fldauth.cls
DOI: 10.1002/fld

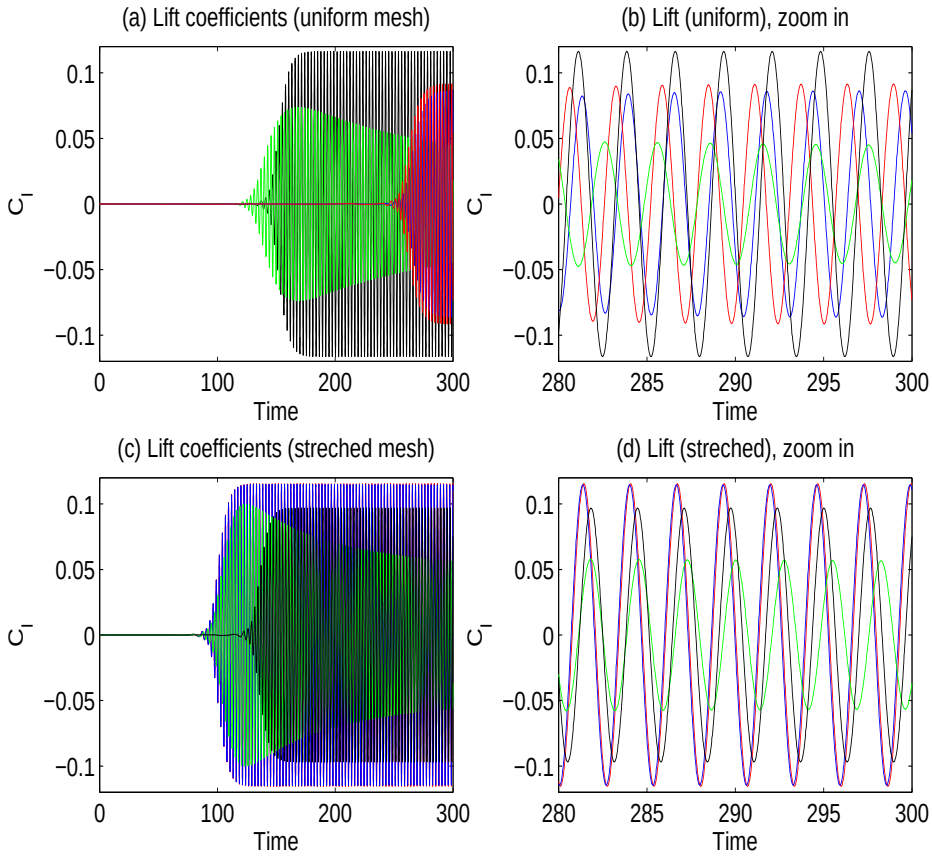

Figure 27. Test problem 3: Lift coefficients.

6. SUMMARY

We have developed a fast and robust computational strategy for finding the numerical solution of models of incompressible flow using implicit methods in conjunction with a stabilized spatial approximation method. We have demonstrated the effectiveness of this solution algorithm on a series of benchmark problems, where it is shown in particular that very little preliminary knowledge of problem structure or parameter tuning is needed to efficiently compute accurate solutions. We have also considered the design of an appropriate stabilization parameter within the stabilized $\boldsymbol{Q}_1$–$\boldsymbol{P}_0$ methodology. Our experiments show that $\beta^\star = \frac{1}{4}\nu$ is the appropriate scaling. This means that the requirement for spatial stabilization of $\boldsymbol{Q}_1$–$\boldsymbol{P}_0$ approximation is reduced as the Reynolds number is increased. For the test problems considered here the unstabilized $\boldsymbol{Q}_1$–$\boldsymbol{P}_0$ approach appears to be a perfectly effective discretization strategy.

REFERENCES

1. Roos HG, Stynes M, Tobiska L. *Robust Numerical Methods for Singularly Perturbed Differential Equations, Second Edition*. Springer: Berlin, 2008. ISBN: 978-3-540-34466-7.

Prepared using fldauth.cls
DOI: 10.1002/fld

2. Liao Q. Error estimation and stabilization for low order finite elements. Ph.D thesis, The University of Manchester 2010.
3. Kay D, Gresho P, Griffiths D, Silvester D. Adaptive time-stepping for incompressible flow; part II: Navier-Stokes equations. *SIAM J. Sci. Comput.* 2010; **32**:111–128.
4. Simo JC, Armero F. Unconditional stability and long-term behaviour of transient algorithms for the incompressible Navier-Stokes and Euler equations. *Comput. Methods Appl. Mech. Engrg.* 1994; **111**:111–154.
5. Elman H, Silvester D, Wathen A. *Finite Elements and Fast Iterative Solvers: with Applications in Incompressible Fluid Dynamics*. Oxford University Press: Oxford, 2005. Xiv+400 pp. ISBN: 978-0-19-852868-5; 0-19-852868-X.
6. Gresho P, Sani R. *Incompressible Flow and the Finite Element Method: Volume 2: Isothermal Laminar flow*. John Wiley: Chichester, 1998.
7. Kechkar N, Silvester D. Analysis of locally stabilized mixed finite element methods for the Stokes problem. *Math. Comp.* 1992; **58**:1–10.
8. Silvester D. Optimal low order finite element methods for incompressible flow. *Comput. Methods Appl. Mech. Engrg* 1994; **111**:357–368.
9. Bochev P, Gunzburger M, Lehoucq R. On stabilized finite element methods for the Stokes problem in the small time step limit. *Int. J. Numer. Meth. Fluids* 2007; **53**:573–597.
10. Burman E, Fernández M. Galerkin finite element methods with symmetric pressure stabilization for the transient Stokes equations: Stability and convergence analysis. *SIAM J. Numer. Anal*. 2008; **47**:409–439.
11. Silvester D, Elman H, Ramage A. Incompressible Flow and Iterative Solver Software (IFISS) version 3.1 January 2011. Available online at `http://www.manchester.ac.uk/ifiss`.
12. Gresho P, Gartling D, Torczynski J, Cliffe K, Winters K, Garratt T, Spence A, Goodrich J. Is the steady viscous incompressible 2d flow over a backward facing step at re=800 stable? *Int. J. Numer. Meth. Fluids* 1993; **17**:501–541.
13. Barton I. The entrance effect of laminar flow over a backward-facing step geometry. *Int. J. Numer. Meth. Fluids* 1997; **25**:633–644.
14. Barrenechea G, Blasco J. Pressure stabilization of finite element approximations of time-dependent incompressible flow problems. *Comput. Methods Appl. Mech. Engrg.* 2007; **197**:219231.
15. Gartling D. A test problem for outflow boundary conditions - flow over a backward-facing step. *Int. J. Numer. Meth. Fluids* 1990; **11**:953–967.
16. Elman H, Ramage A, Silvester D. Algorithm 866: IFISS, a Matlab toolbox for modelling incompressible flow. *ACM Trans. Math. Softw.* 2007; **33**:2–14.
17. Sharma A, Eswaran V. Heat and fluid flow across a square cylinder in the two-dimensional laminar flow regime. *Num. Heat Transfer* 2004; **Part A 45**:247–269.

DOI: 10.1002/fld